Turbine Powered Simulator Calibration and Testing for Hybrid Wing Body Powered Airframe Integration

Patrick R. Shea* and Jeffrey D. Flamm†
NASA Langley Research Center, Hampton, VA 23681, USA

Kurtis R. Long‡ and Kevin D. James§
NASA Ames Research Center, Moffett Field, CA 94035, USA

Daniel M. Tompkins¶ and Michael D. Beyar‖
The Boeing Company, Huntington Beach, CA 92647, USA

Propulsion airframe integration testing on a 5.75% scale hybrid wing body model using turbine powered simulators was completed at the National Full-Scale Aerodynamics Complex 40- by 80-foot test section. Four rear control surface configurations including a no control surface deflection configuration were tested with the turbine powered simulator units to investigate how the jet exhaust influenced the control surface performance as related to the resultant forces and moments on the model. Compared to flow-through nacelle testing on the same hybrid wing body model, the control surface effectiveness was found to increase with the turbine powered simulator units operating. This was true for pitching moment, lift, and drag although pitching moment was the parameter of greatest interest for this project. With the turbine powered simulator units operating, the model pitching moment was seen to increase when compared to the flow-through nacelle configuration indicating that the center elevon and vertical tail control authority increased with the jet exhaust from the turbine powered simulator units.

Nomenclature

Abbreviations

CN1	Model configuration – No control surface deflections
CN2	Model configuration – -30° Elevon 1/2 deflection
CN3	Model configuration – -40° Elevon 1/2 deflection
CN4	Model configuration – -40° Elevon 1/2 and full vertical tail deflections
P1	Low TPS power setting – $FNPR = 1.040$
P2	Intermediate TPS power setting – $FNPR = 1.100$
P3	High TPS power setting – $FNPR = 1.362$
AIP	Aerodynamic Interface Plane
BPR	Bypass Ratio
BWB	Blended Wing Body
FTN	Flow-Through Nacelle
HPA	High Pressure Air

*Aerospace Engineer, Configuration Aerodynamics Branch, Mail Stop 499, AIAA Member.
†Aerospace Engineer, Configuration Aerodynamics Branch, Mail Stop 499, AIAA Associate Fellow.
‡Research Engineer, Experimental Aero-Physics Branch, Mail Stop 260-1, AIAA Member.
§Aerospace Engineer, Experimental Aero-Physics Branch, Mail Stop 260-1, AIAA Associate Fellow.
¶Propulsion Engineer, Boeing Research & Technology, 14900 Bolsa Chica Rd., AIAA Senior Member.
‖Aerodynamics Engineer, Boeing Research & Technology, 14900 Bolsa Chica Rd., AIAA Member.

HWB	Hybrid Wing Body
NFAC	National Full-Scale Aerodynamics Complex
PAI	Propulsion Airframe Integration
TPS	Turbine Powered Simulator
UHB	Ultra-High Bypass
UPWT	Unitary Plan Wind Tunnel

Symbols

Δ	Difference

Variables

α	Angle of attack
C_D	Drag coefficient
C_L	Lift coefficient
C_m	Pitching moment coefficient
$CNPR$	Core nozzle pressure ratio
$FNPR$	Fan nozzle pressure ratio
FPR	Fan pressure ratio
FR	Resultant force
NC	Corrected fan rotational speed
q	Dynamic pressure
WC_2	Corrected fan weight flow
σ	Standard deviation

I. Introduction

I.A. HWB Background

The hybrid wing body (HWB), also referred to as the blended wing body (BWB), is an aircraft with the wings aerodynamically blended to the main body while still maintaining distinct wing and body structures. The original design concepts of the HWB as a subsonic transport aircraft date back to the 1980s and were developed in an effort to advance aircraft design beyond the common tube and wing configuration. Initial design assessments indicated that an HWB aircraft could be lighter, have a higher lift-to-drag ratio, and could reduce fuel burn when compared to a conventional aircraft designed for the same mission.[1] As the HWB has evolved, numerous ground and flight tests have been performed (e.g., references 2,3,4,5,6, or 7) to evaluate the aerodynamic performance and flight characteristics of the HWB geometry. The current studies look to advance the study of the HWB airframe with a specific focus on propulsion airframe integration (PAI).

The Environmentally Responsible Aviation (ERA) Project within the NASA Aeronautics Research Mission Directorate (ARMD) had the responsibility to evaluate and document air vehicle concepts and enabling technologies that have the potential to reduce the environmental impact of aviation. Within the ERA Vehicle Systems Integration subproject, the ultra-high bypass ratio (UHB) Engine integration for hybrid wing bodies technology demonstration was established to evaluate engine/airframe integration on HWB system performance and engine operability. The goal of these efforts was to demonstrate an HWB PAI design concept that could enable fuel burn reductions in excess of 50% while providing noise shielding to reduce noise propagation. NASA partnered with Boeing to design and verify an HWB PAI concept that minimized adverse propulsion/airframe induced interference effects that could result in high drag or poor aerodynamic characteristics. A 5.75% scale model[8] of the HWB concept was evaluated in a series of tests including flow-through nacelle tests for assessment of the airframe stability and control,[9] powered ejector test to investigate engine inlet flow fields and distortion at the aerodynamic interface plane (AIP),[10] and turbine powered simulator (TPS) testing to study power effects on the airframe with a focus on control surface performance.

I.B. Turbine Powered Simulator Testing

Turbine powered simulators have been used for the past several decades for PAI testing (e.g., references 11,12,13 or 14). The TPS units selected for the current tests were originally designed for traditional airframe testing with the motors mounted below the wing on pylons. In this study, the motors were mounted on the

upper surface of the HWB configuration. A risk reduction test was performed at the NASA Ames Unitary Plan Wind Tunnel (UPWT) 11- by 11-foot Transonic Test Section to ensure that the units would operate as expected when inverted. Of particular concern was the ability to supply lubrication oil to the motors. Additionally, these tests provided the opportunity to evaluate new fan nozzle geometries developed for simulating the UHB configuration. Upon successful completion of the risk reduction tests in 2013, the final design of the HWB test article was able to move forward.[15]

II. Turbine Powered Simulator Calibration

II.A. Experimental Setup

Calibration of three matched TPS units was performed at the NASA Ames UPWT 9- by 7-foot Supersonic Test Section to evaluate the performance characteristics of each of the units in static conditions. The turbofan simulator cores were Tech Development, Inc. (TDI) Model 2700 TPS units, which consisted of a 0.5 ft diameter fan turning on a shaft driven by a two stage turbine, which itself was powered by high pressure air. To these TPS cores were added inlets, exhaust nozzles and interior flowpath components designed by Boeing for this test program.[15] Originally designed for low bypass ratio (BPR), high fan pressure ratio (FPR) applications, the TPS cores were operated with these redesigned inlets, nozzles, and flowpath components to simulate the pressure ratios of a UHB engine as required for the HWB test program. Multiple hardware configurations were tested including three different core units (indicated as Motors 1–3) and three different fan nozzle exit areas. The TPS units were instrumented with pressure and temperature rakes in the fan and core flows to monitor performance during testing, and were mounted to a test stand instrumented with a six-component flow-through balance to evaluate forces generated during operation over a wide range of fan pressures, core pressures, and operational speeds.[16,17] Figure 1 shows one of the TPS units installed in the test chamber on the sting mounted test stand. Note that the bellmouth attached to the front of the unit was only used for calibration and the bellmouth itself was calibrated using CFD (StarCCM+) to establish the relationships between static pressure measured in the bellmouth and mass flow rate.

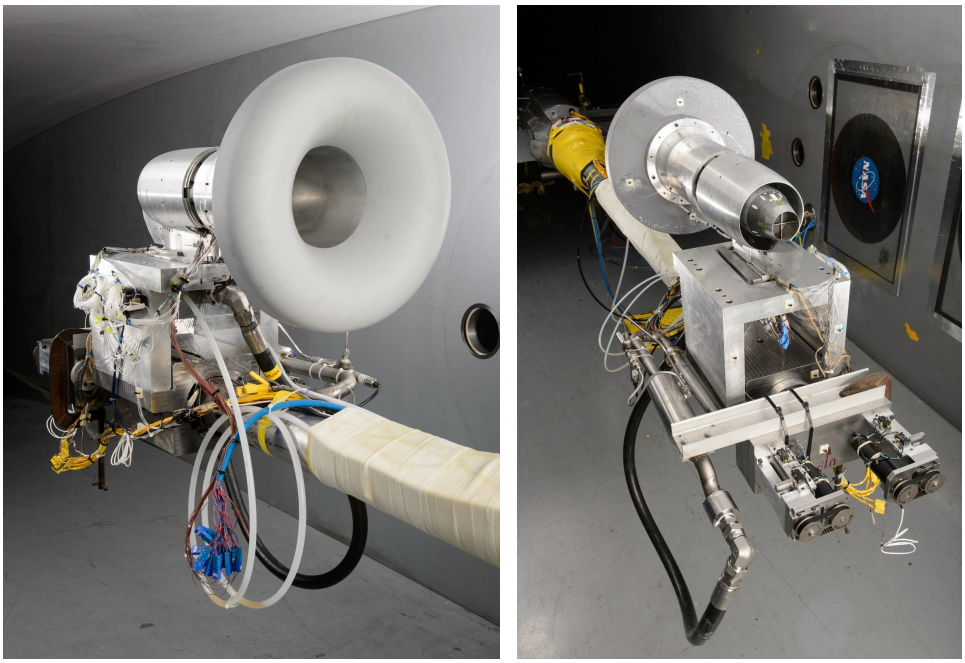

(a) Front View (ADC14-0224-007) (b) Aft View (ADC14-0224-002)

Figure 1. TPS calibration setup in the NASA Ames UPWT 9- by 7-foot Supersonic Test Section.

II.B. Calibration Map Development

Figures 2 & 3 show results from the TPS calibration tests. Two of the operational characteristics of interest are the resultant force (FR) developed by the motor and the sea level corrected weight flow ingested by the fan (WC_2, measured using the calibrated bellmouth discussed previously). Figure 2 shows FR over a range of fan pressure ratios (FPR) and corrected rotational speeds (indicated as NC). Multiple runs for each of the three TPS cores are plotted on each figure and show good agreement. Similar plots are shown in figure 3 for WC_2, and again good agreement is seen for each of the motors for several repeated runs.

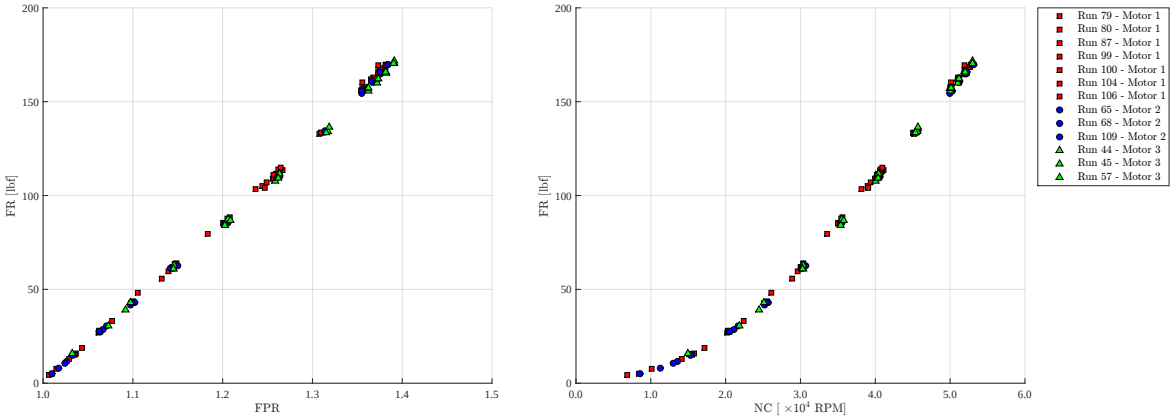

(a) Function of FPR (b) Function of NC

Figure 2. Chart of TPS resultant force (FR).

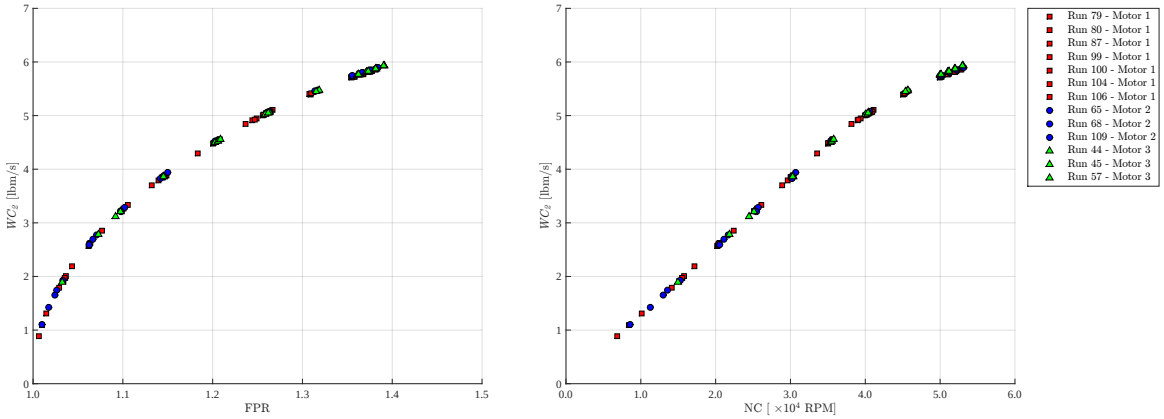

(a) Function of FPR (b) Function of NC

Figure 3. Chart of TPS fan weight flow (WC_2).

The raw data from the calibration tests were used to develop a set of lookup algorithms that were used to estimate the TPS performance during PAI testing on the HWB model, as direct measures of the resultant force and fan weight flow were not possible during integrated testing. The basic procedure is outlined in the sections below.

II.B.1. Force Corrections

The calibrations were intended to be performed at static conditions, however, the TPS units generated enough flow to cause freestream flow in the tunnel test section. To account for this, the freestream velocity was monitored with a rotating vane anemometer located several fan diameters upstream of the TPS unit, and the calibration test stand and bellmouth were instrumented with pressure transducers to evaluate base

drag. Three corrections were made to the force measurements to account for the freestream velocity: base drag on the bellmouth, base drag on the test stand, and ram drag.

II.B.2. Map data to uniform NC values

The next step in developing the lookup tables was to develop relationships for FPR, WC_2, and FR at prescribed motor speeds (NC). The data were sorted by fan nozzle area (0.104, 0.111, or 0.118 ft^2) and 4^{th} order polynomial fits were used to develop relationships for FPR, WC_2, and FR as functions of NC. These fits were then used to calculate FPR, WC_2, and FR at the prescribed NC values.

II.B.3. Map data to uniform FNPR values

WC_2 and FR were calculated at prescribed values of FPR. This calculation was performed at fixed values of NC using a 2^{nd} order polynomial fit. This resulted in relationships for WC_2 and FR as functions of FPR for each of the prescribed values of NC. At this point in the process, relationships were in place to map between the input parameters (FPR and NC) and the output parameters (WC_2 and FR).

II.B.4. Generate WC_2 and FR lookup algorithms

With the mapping completed in the previous steps, estimated values of WC_2 and FR were defined on a uniform grid of FPR and NC. Intrinsic MATLAB functions were used to perform interpolation of these data to calculate WC_2 and/or FR at any value of FPR and NC inside the grid range used for the mapping. The mapped data were stored in arrays such that simple lookup routines referenced the interpolated arrays as opposed to performing the interpolation every time the desired value of FPR and/or NC changed.

The final stored maps are represented graphically as contour plots seen in figure 4 where the black dots represent the original calibration data that were used to generate the maps. It is important to note that not all of the values presented in the contour plots represent physically realizable operating conditions for the TPS units. For example, it is not possible to achieve high FPR values without spinning the TPS units as depicted in the upper left-hand corner (e.g., $NC = 0$ and $FPR = 1.6$) of the contour plots. Although it is possible to extrapolate to these bounds mathematically to estimate FR and WC_2, the fan maps were monitored regularly during integration testing to ensure that the TPS units were operating within the previously calibrated ranges indicated by the black curves. Also note that the white regions in the contour plots represent negative values of FR and WC_2, which are non-physical during TPS operation.

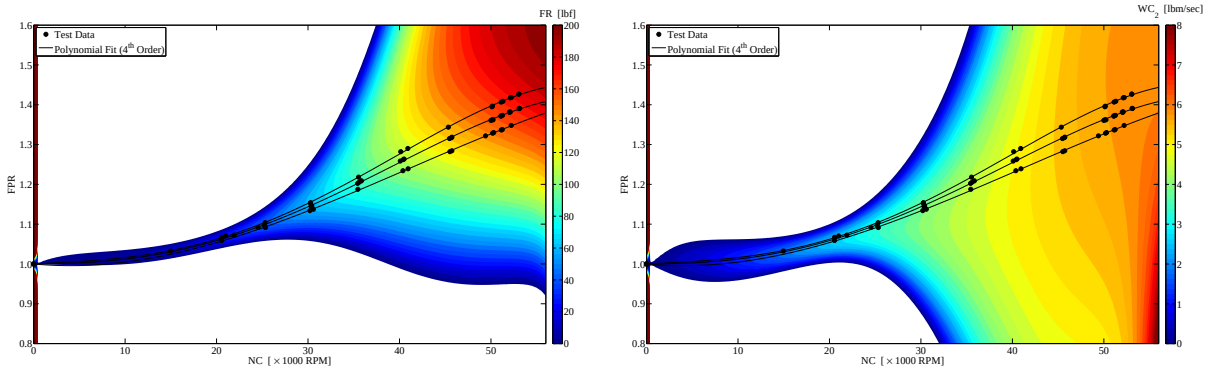

(a) FR (b) WC_2

Figure 4. Contour plots of an example calibration map.

III. Propulsion Airframe Integration Testing

III.A. Facility Overview

The National Full-Scale Aerodynamics Complex (NFAC) is located at NASA Ames Research Center and is operated by the U.S. Air Force's Arnold Engineering Development Complex. The NFAC is an atmospheric

wind tunnel comprised of two test sections, the closed return 40- by 80-foot test section and the open return 80- by 120-foot test section, which both utilize the same fan drive system. A schematic of the facility layout can be seen in figure 5. The 40- by 80-foot test section has an acoustically treated, elliptical test section with a total width of 79 ft and a height of 39 ft. Freestream velocities in the 40- by 80-foot test section range up to 300 knots (506 ft/s), which corresponds to a Reynolds numbers per foot of 3.0×10^6.[18,19,20] For the current tests, the tunnel was operated at a dynamic pressure, q, of 60 lb/ft^2, which corresponds to Mach 0.2 and a freestream velocity of approximately 230 ft/s.

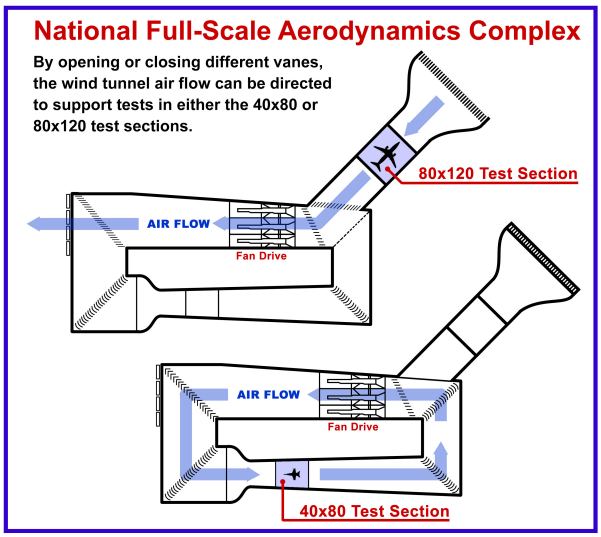

Figure 5. Schematic of the NFAC complex.

III.B. Hybrid Wing Body Model

The PAI test article was a 5.75% geometrically scaled version of the Boeing Blended-Wing-Body BWB-0009G configuration designed to accommodate flow-through nacelle (FTN) testing,[9] inlet distortion testing using ejectors,[10] and engine exhaust plume testing using the TPS units discussed previously. The model had a reference area of 26.833 ft^2, a reference span of 12.228 ft, and a mean aerodynamic chord of 3.717 ft. The Reynolds number, based on the mean aerodynamic chord, was approximately 5.1×10^6. A tri-view of the basic model configuration with flow-through nacelles installed can be seen in figure 6 with the moment reference center indicated on the top and side views using the ◕ symbol. More details on the design and development of the test article can be found in reference 8.

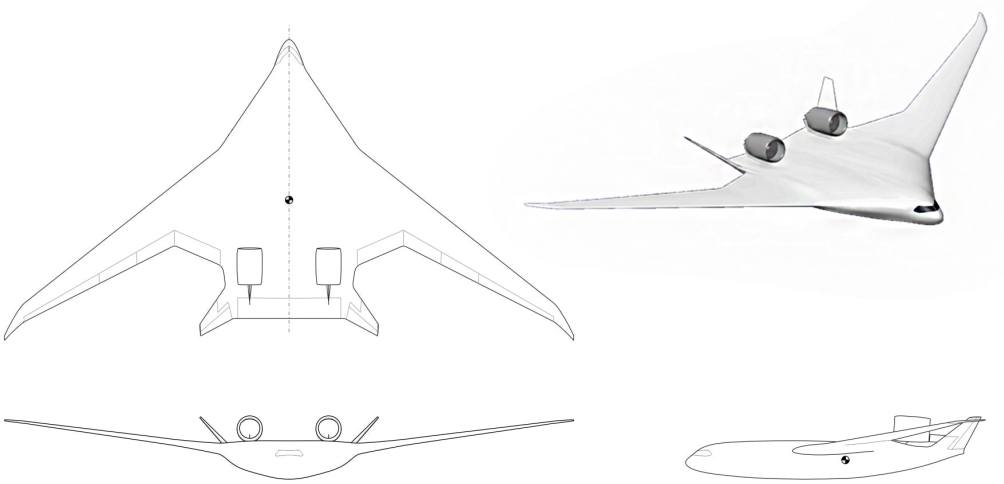

Figure 6. Tri-view of the 5.75% HWB model.

The fully instrumented model was supported via a sting and elbow configuration used to mount the model on an internal, flow-through balance. The sting was attached to the NFAC two degree of freedom (pitch and yaw) model support system. The sting support was not capable of plunge and therefore, did not hold the model centered in the tunnel during pitch sweeps. Similarly, the model was not centered over the yaw table and the model was not centered in the tunnel during sideslip sweeps. The wall effects resulting from the model not remaining centered in the test section were evaluated using CFD simulations (StarCCM+) of the wind tunnel contraction, test section, diffuser, the HWB model, and the model support hardware. The results from these simulations indicated that the wall effects were negligible as predicted due to the small scale and low blockage of the test model relative to the large test section. The installed model with TPS units can be seen in figure 7.

Figure 7. HWB model installed in the NFAC 40- by 80-foot test section with TPS units. (ACD15-0138-002)

III.B.1. Control Surfaces

The HWB model was designed to test a wide array of control surface deflections to evaluate stability and control in both the FTN and TPS configurations. Figure 8 provides an overview of the control surface locations and the naming convention. For the TPS tests, control surface deflections were limited to the center elevon (1/2) and the vertical tails. Table 1 provides an overview of the specific configurations tested. Note that the elevon 1/2 deflections were always into the path of the TPS exhaust (figure 9(a)), and that both vertical tails were deflected towards the center of the aircraft (figure 9(b)). A leading-edge Krueger flap was also deployed in a single configuration for all of the TPS testing. This configuration had the Krueger set to a 40° deflection, and was sealed between the trailing edge of the flap and the leading edge of the wing using foil tape.

III.C. Turbine Powered Simulator Configurations

The TPS units used for the current tests were modified to simulate exhaust flow representative of a full-scale ultra-high bypass gas turbine engine. For PAI testing at the NFAC, the fan exit area was fixed at 0.111 ft^2. The TPS units were operated at three power settings including a low power setting that was selected as

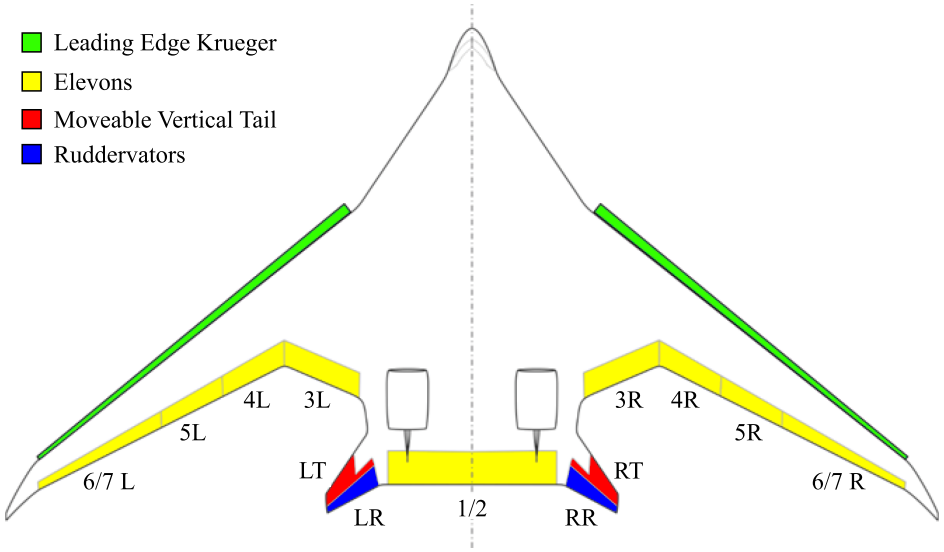

Figure 8. HWB model control surface layout.

Table 1. Control surface deflection configurations. All deflections are in degrees.

Configuration	Left V-Tail (LT)	Left Rudder (LR)	Elevon 1/2	Right Rudder (RR)	Right V-Tail (RT)
CN1	0	0	0	0	0
CN2	0	0	-30	0	0
CN3	0	0	-40	0	0
CN4	-15	-30	-40	-30	-15

the lowest operable speed with a repeatable *FPR* greater than 1.000, an intermediate power setting, and a high power setting intended to model the full-scale engine. A table of these power settings and relevant parameters can be seen in Table 2. Figure 10 shows the typical plumes that developed downstream of the TPS units during operation. Note that *FPR*, *FNPR*, and *CNPR* were measured using five pressure rakes in the fan flow and four pressure rakes in the core flow of each TPS unit. At each of the nine rake (five in the fan, four in the rake) stations, calibrated thermocouples[21] were used to monitor temperatures.

Table 2. Nominal conditions for three TPS power settings tested.

Setting	*FNPR*	*CNPR*	*NC* [rpm]
P1	1.040	1.013	13,100
P2	1.100	1.034	23,500
P3	1.362	1.276	47,000

The three power settings were achieved by adjusting the high pressure air (HPA) supplied to the model. HPA was supplied through the sting and flow-through balance. In order to supply air to the two independent TPS units, the air was split via a manifold inside of the model that was attached to the model balance block. Downstream of the manifold on the HPA supply lines, independently controllable needle valves were put in place so that fine adjustments could be made to the two supply air pressures to ensure the two TPS units were operating at the same nominal conditions. Venturi flow meters, pressure transducers, and thermocouples were installed in the model upstream of the TPS units to help monitor the high pressure air supplied to each TPS unit. Two TPS heights above the surface of the model (that is, two pylon lengths) were evaluated during testing. The nominal (high) TPS results are presented in the following sections with the exception of Section III.D.5 where the two height settings are compared directly.

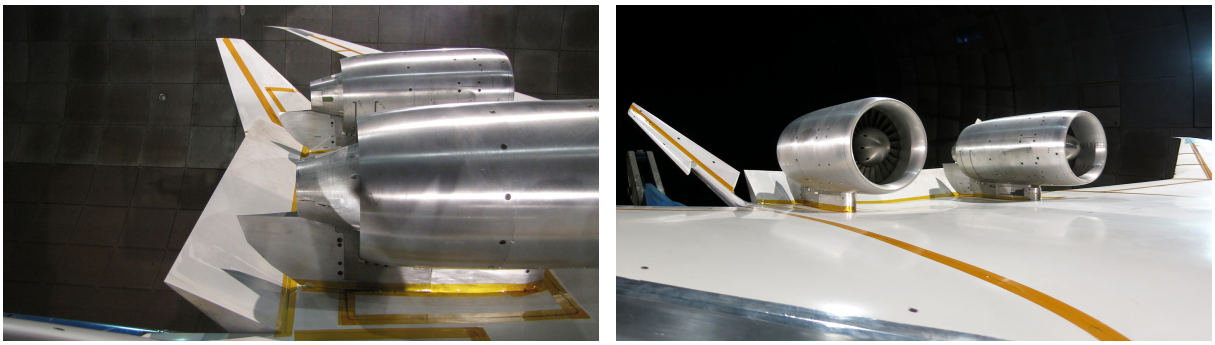

(a) Elevon 1/2 Only (b) Elevon 1/2 and Vertical Tails

Figure 9. Examples of control surface deflections evaluated during TPS tests.

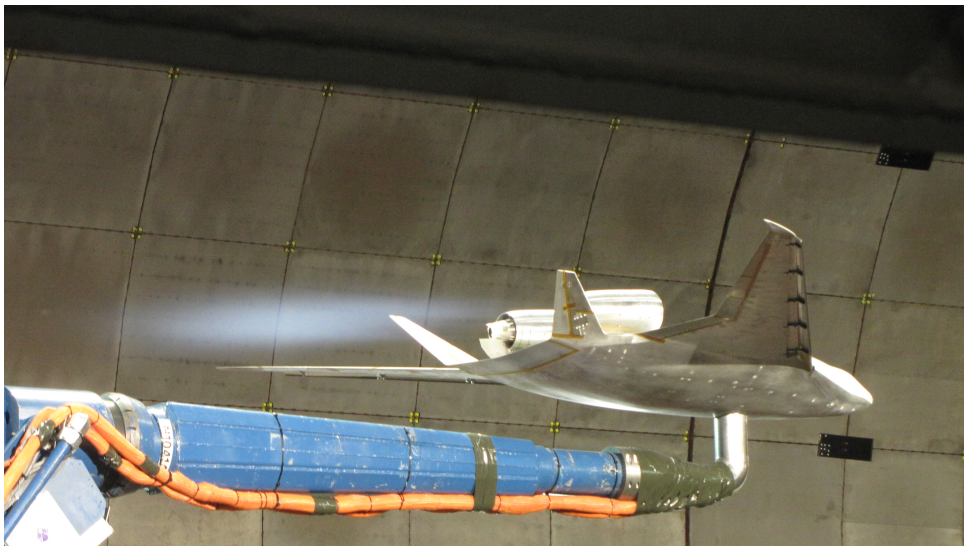

Figure 10. Photo of the TPS exhaust plumes during PAI testing on the HWB model.

III.D. Propulsion Airframe Integration Results

The focus of these efforts was to determine the stability and control characteristics of the HWB with the TPS units operating. As such, the data presented in the following section have been corrected in an effort to remove the force and moments directly related to the TPS units to arrive at the aerodynamic forces and moments on the HWB model. These corrections include removing the thrust (FR estimated from the calibration) and ram drag (calculated based on estimates from the calibration of WC_2). All of the data presented here were acquired at zero sideslip angle.

III.D.1. Comparison to FTN

Figure 11 compares the results from the FTN and high power TPS ($P3$) installations. Figure 11 shows pitching moment coefficient (C_m), lift coefficient (C_L), and drag coefficient (C_D) as functions of angle of attack as well as the drag polar (C_L as a function of C_D). Looking at pitching moment (top left) and drag (bottom right), the TPS cases are consistently lower than the FTN test cases. These two measurements will be related due to the position of the TPS units on the upper surface of the model. Consider a test case with no freestream flow and the TPS units operating at maximum power. At these conditions, the thrust of the TPS units will generate a positive axial force (negative drag) and a nose down (negative) pitching moment. Considering the test case with no freestream flow and noting that the reduced drag was unexpected for the TPS configuration, there is a possibility that the force and moment corrections are underestimating thrust or overestimating ram drag. Conversely, the flow-through nacelles will also generate small levels of thrust and

ram drag, which were not accounted for and could potentially account for the difference seen between the two data sets. C_L will be relatively insensitive to thrust and ram drag, and therefore, the positive increment as compared to the FTN configurations is most likely attributed to increasing the flow velocity over the suction surface of the model centerbody.

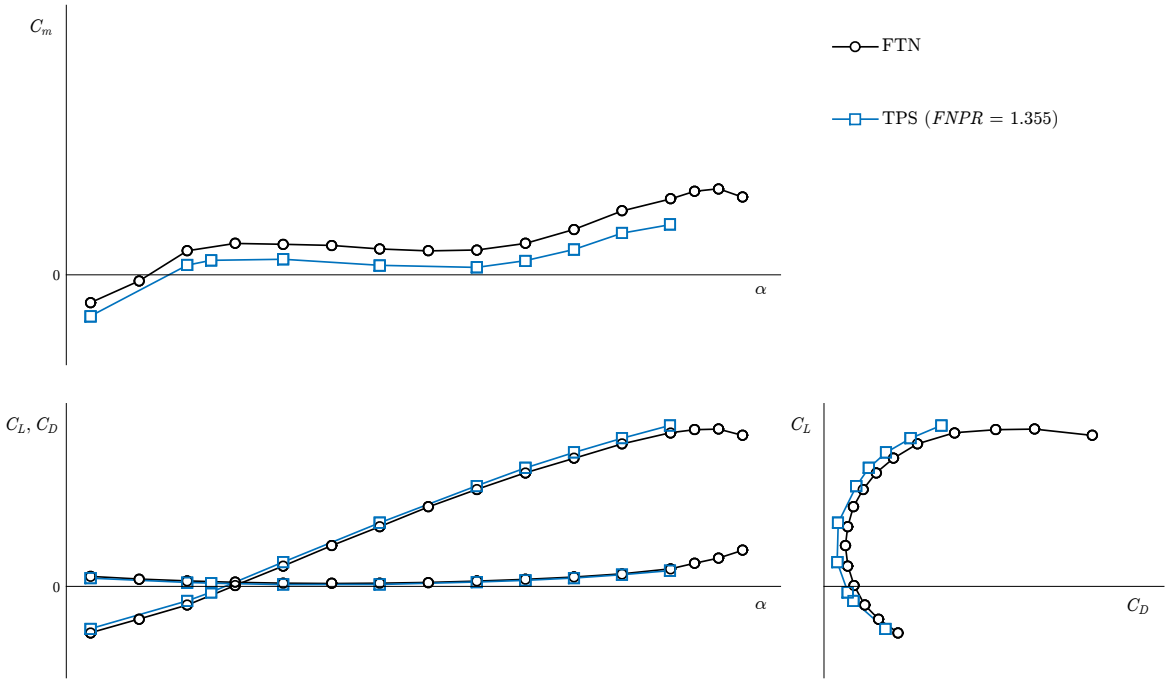

Figure 11. Comparison of FTN and TPS installation effects on lift, drag, and pitching moment with no control surface deflections (*CN1*).

Figures 12–14 compare the results from the FTN and high power TPS (*P3*) installations at the three control surface deflection configurations tested. In general, as the control surface deflections are increased (*CN2* to *CN3* to *CN4*), the increments resulting from the TPS units are seen to decrease in each of the forces and moments. This is most clearly seen in the drag polar where the two curves have nearly collapsed for the *CN4* configuration. Similarly, the C_L increments are reduced with increased control surface deflections although the increments persist at higher angles of attack for each of the configurations. C_m increments between the FTN and TPS are seen as negative for *CN1* and *CN2* and positive for *CN3* and *CN4*, although the magnitude of the increments are seen to decrease as the control surface deflections are increased.

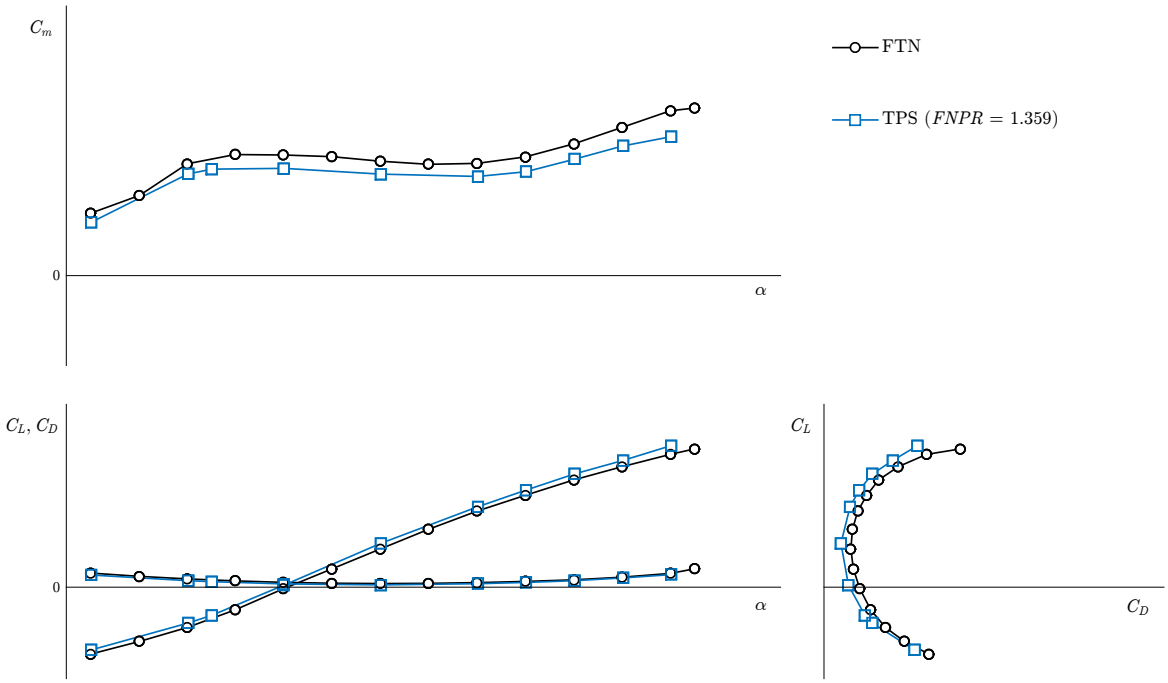

Figure 12. Comparison of FTN and TPS installation effects on lift, drag, and pitching moment with elevon 1/2 deflected -30° (*CN2*).

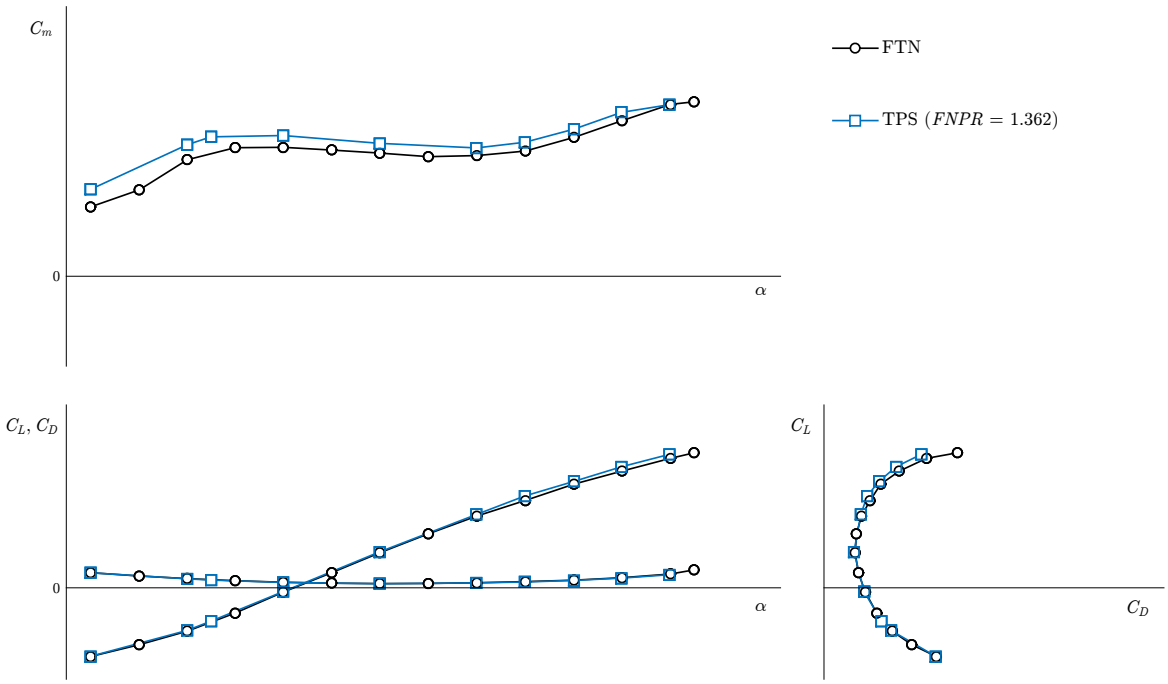

Figure 13. Comparison of FTN and TPS installation effects on lift, drag, and pitching moment with the maximum elevon 1/2 deflection (*CN3*).

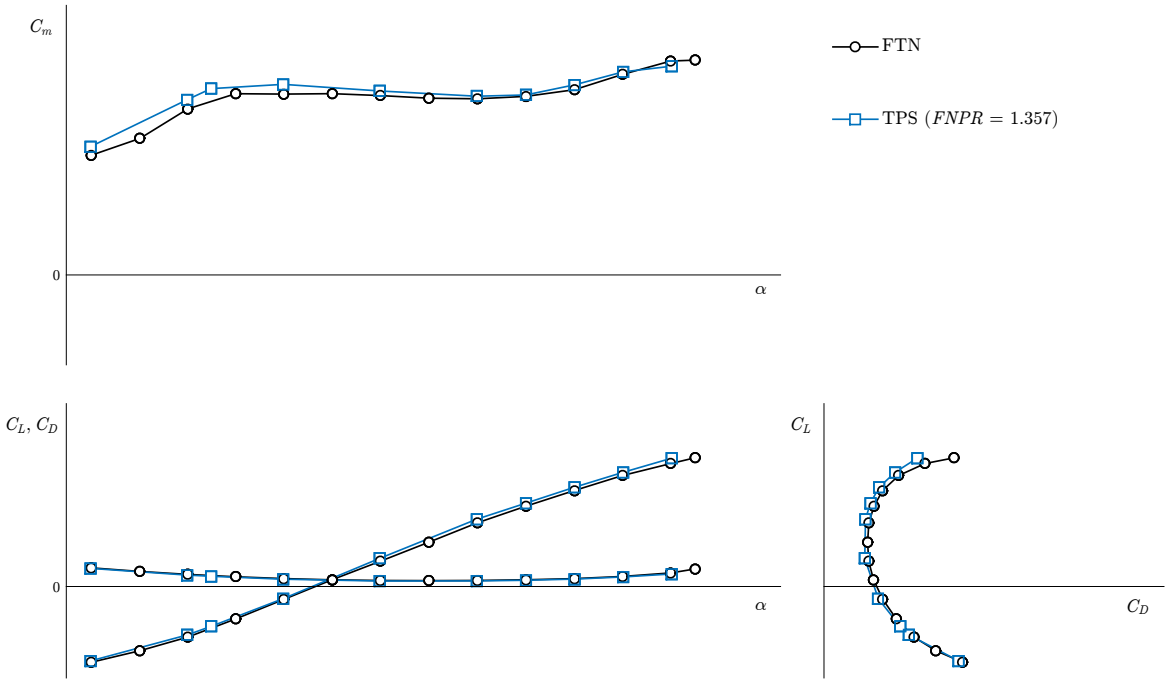

Figure 14. Comparison of FTN and TPS installation effects on lift, drag, and pitching moment with the maximum elevon 1/2 and vertical tail deflections ($CN4$).

III.D.2. Repeatability

An important consideration when comparing the TPS results is the run-to-run repeatability of the same test configuration. Figures 15 & 16 compare C_m, C_L, and C_D for three runs acquired at the same nominal test conditions. These runs were acquired on different days, both with and without model changes between the runs in an effort to assess the data quality. Figure 15 shows good repeatability for C_m, C_L and some variation between the runs for C_D (specifically Repeat 2). Figure 16 shows the differences relative to the mean values along with dotted lines that indicate the 95% confidence bounds (2σ) calculated using all of the pitch sweep data from the three repeats (30 points in total). These confidence bounds are included on all of the differential plots that follow.

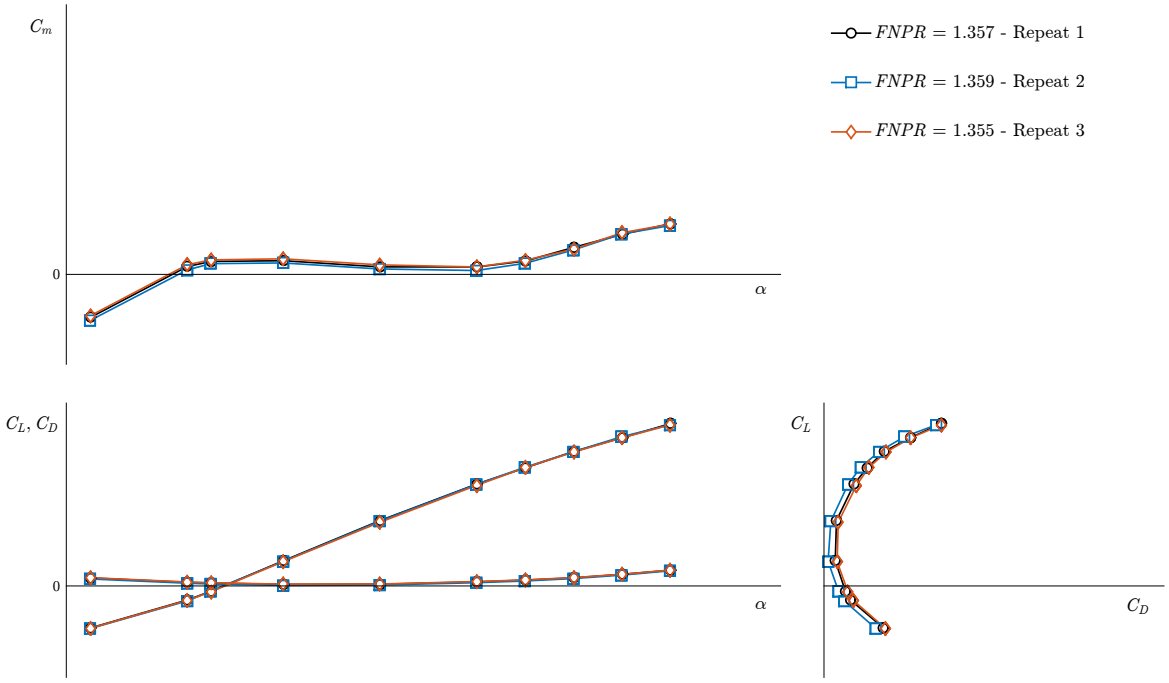

Figure 15. Evaluation of TPS repeatability for lift, drag, and pitching moment at the high power TPS setting (*P3*) with no control surface deflections (*CN1*).

III.D.3. Power Setting Effects

Figures 17 & 18 compare C_m, C_L, and C_D for the *CN1* configuration at three power settings (*P1*, *P2*, and *P3*) and zero sideslip. The data for C_m and C_D are seen to collapse across the range of angles of attack investigated indicating that the thrust and ram drag corrections are working as expected, which may indicate that the FTN data require some correction for thrust and ram drag. Studying C_L, a positive increment is seen throughout the pitch sweep for *P3* relative to *P1* (figure 18). The intermediate power setting (*P2*) starts at a positive increment relative to *P1* at low angles of attack, but this increment does not persist at the higher angles of attack and the curves for *P1* and *P2* collapse. If the TPS units are in fact accelerating the flow over the suction surface of the model at the high power setting (*P3*) and therefore increasing lift, then these results would indicate that the TPS units are unable to accelerate the flow in the presence of the adverse pressure gradient at high angles of attack at the intermediate power setting (*P2*).

Figures 19–24 study the effect of power setting with increasing control surface deflections. As one might expect, the interactions of the TPS exhaust with the control surfaces become more complex as the control surfaces are deflected farther into the exhaust plumes. Starting with the *CN2* configuration (figures 19 & 20), a proportional increment is now seen in the pitching moment as the power setting increases. Interestingly, the drag polars for *P1* and *P3* collapse fairly well, but a decrease in drag is seen for *P2* over a significant portion of the polar. This drag decrease can potentially be attributed to the measurement uncertainty (indicated with the dotted lines on figure 20), but the intermediate power setting (*P2*) is consistently lower in drag for

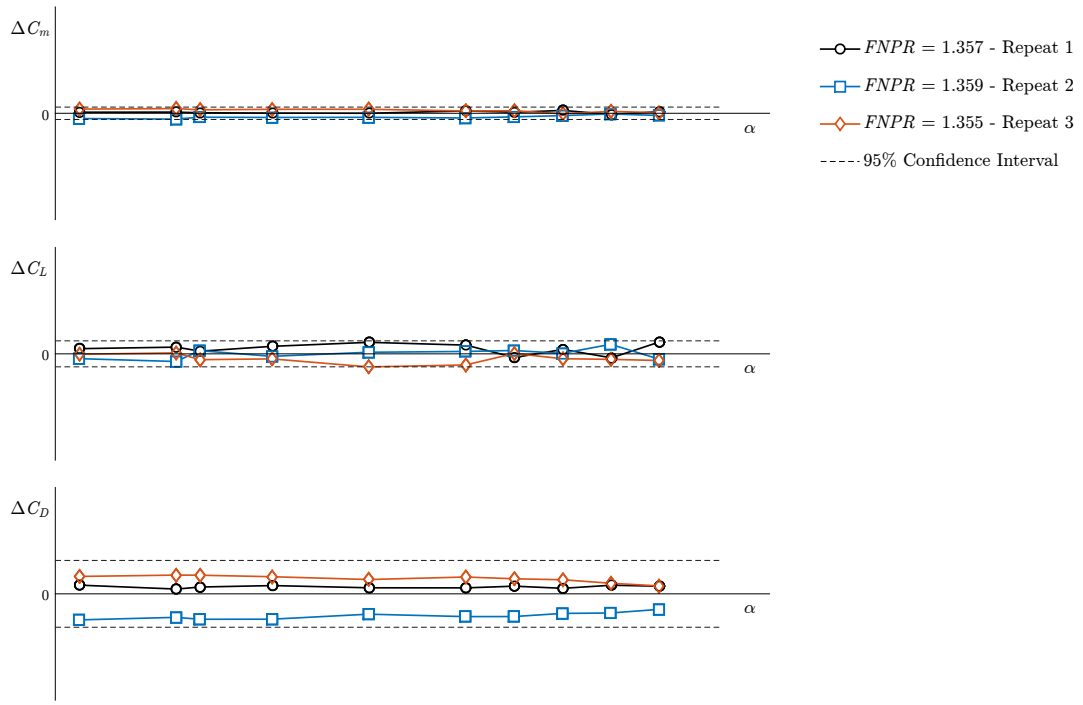

Figure 16. Evaluation of TPS repeatability for lift, drag, and pitching moment at the high power TPS setting (*P3*) with no control surface deflections (*CN1*). Differential values referenced to mean.

each of the configurations investigated indicating that the trend may be physical. The *CN2* results for C_L closely resemble those for the *CN1* configuration with a relatively uniform positive increment for *P3* relative to *P1* and a positive increment for *P2* relative to *P1* that decreases in magnitude at high angles of attack.

The *CN3* configuration results are seen in figures 21 & 22. A significant positive increment is now seen in C_m for the high power setting that is nearly uniform across the pitch sweep. A small positive increment is also seen for *P2* relative to *P1*. The drag polar displays more complex behavior. In general, drag decreased at the intermediate power setting and increased at the highest power setting. Studying C_L, the curves for *P1* and *P3* effectively collapse, but *P2* has a unique trend that includes a positive lift increment at low angles of attack and a negative lift increment at the highest angles of attack, relative to *P1* and *P3*. Including more power settings in the power sweep would offer more insight into how the lift and drag are affected by the control surface/exhaust plume interactions.

Similar trends to *CN3* are seen in the *CN4* configuration results (figures 23 & 24). Increasing positive increments for the pitching moment are seen with increasing power. The drag polar again indicates a decrease in drag for *P2* and an increase in drag for *P3*. Finally, the C_L curves for *P1* and *P3* effectively collapse, and *P2* has a positive lift increment at low angles of attack, relative to *P1* and *P3*, and a negative lift increment at the highest angles of attack similar to the *CN3* configuration.

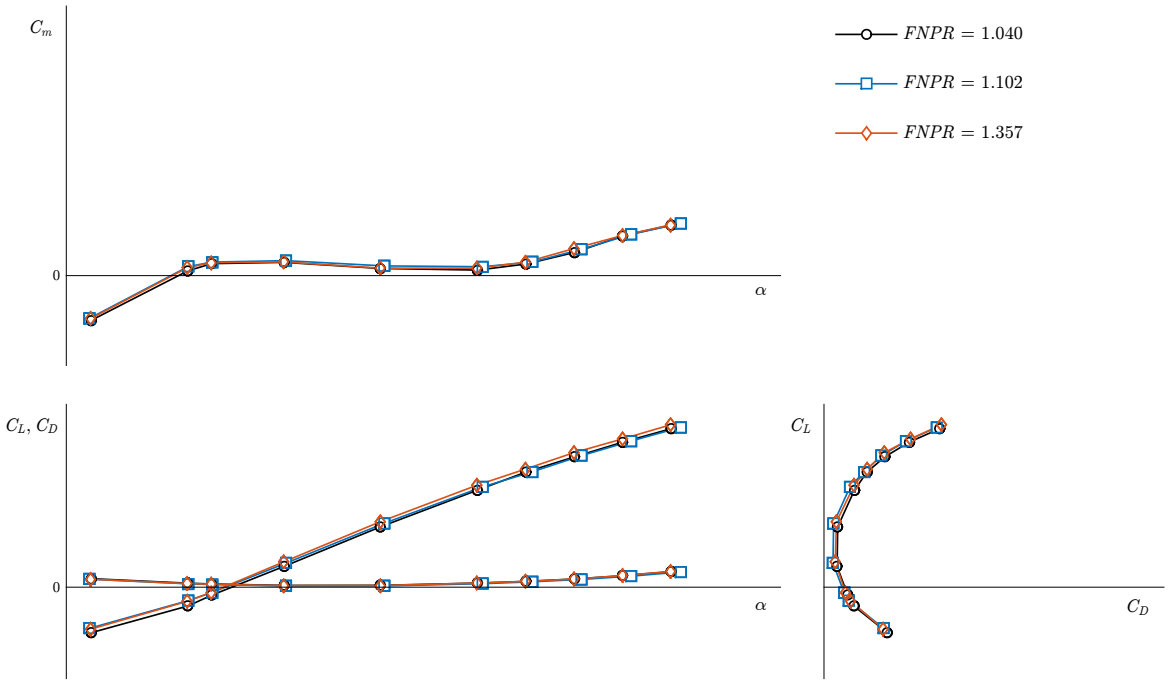

Figure 17. Comparison of TPS power setting effects on lift, drag, and pitching moment with no control surface deflections (*CN1*).

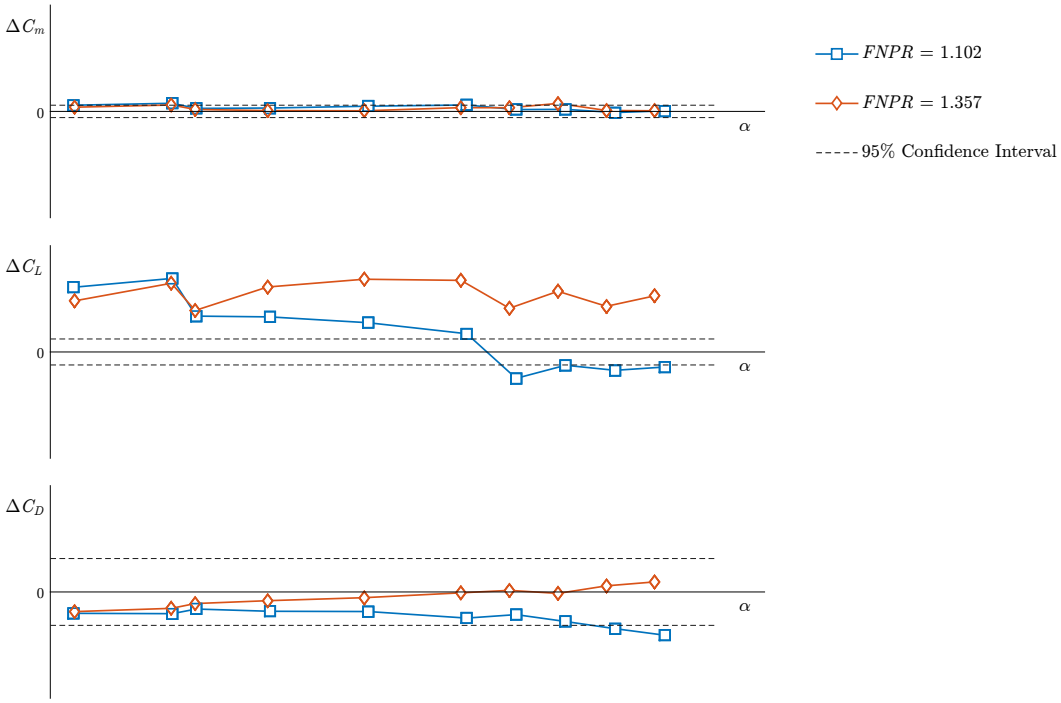

Figure 18. Comparison of TPS power setting effects on lift, drag, and pitching moment with no control surface deflections (*CN1*). Confidence intervals taken from repeatability tests (figure 16).

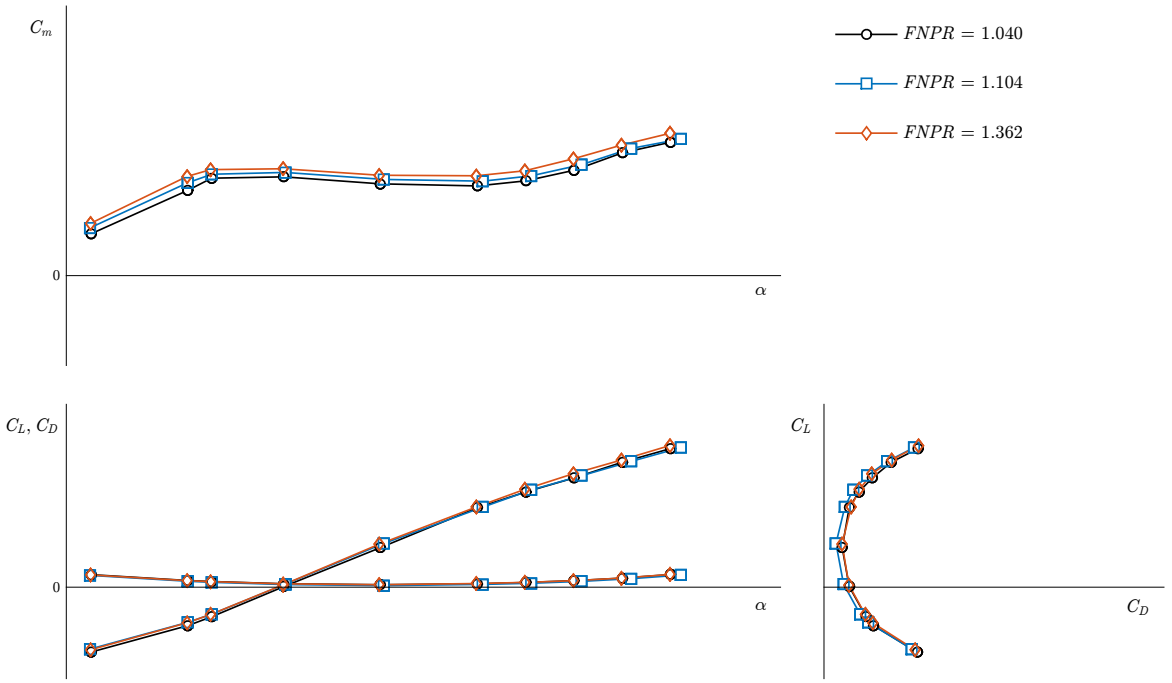

Figure 19. Comparison of TPS power setting effects on lift, drag, and pitching moment with elevon 1/2 deflected -30° (*CN2*).

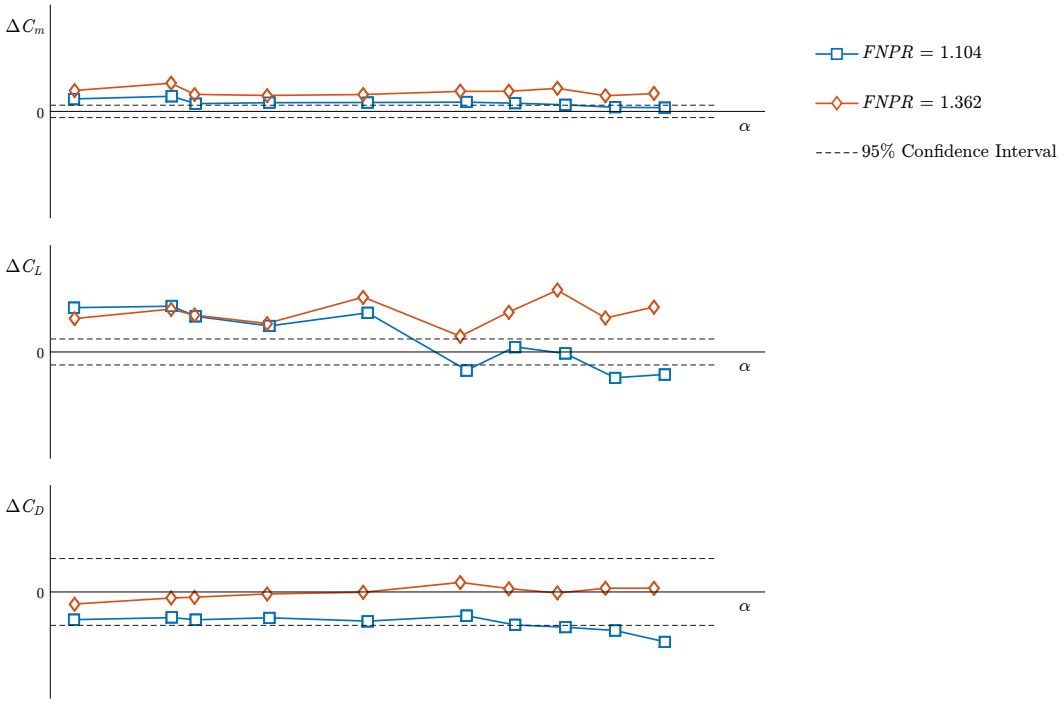

Figure 20. Comparison of differential lift, drag, and pitching moment with elevon 1/2 deflected -30° (*CN2*). Low power TPS data (*P1*) used as differential reference. Confidence intervals taken from repeatability tests (figure 16).

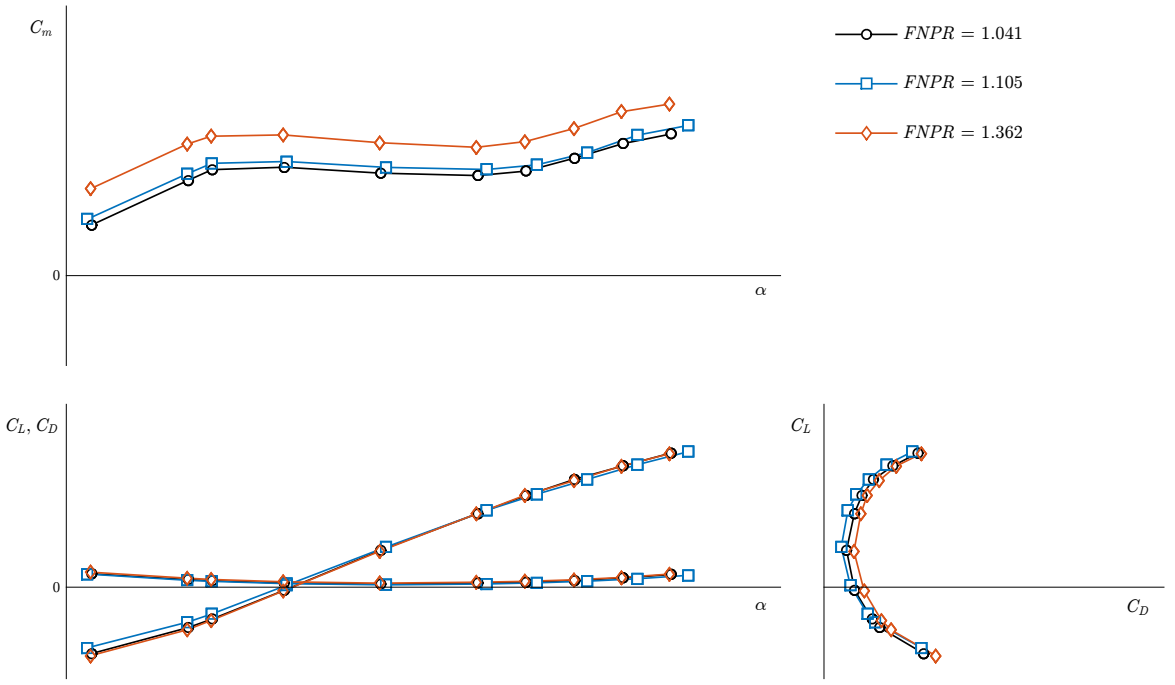

Figure 21. Comparison of TPS power setting effects on lift, drag, and pitching moment with the maximum elevon 1/2 deflection (*CN3*).

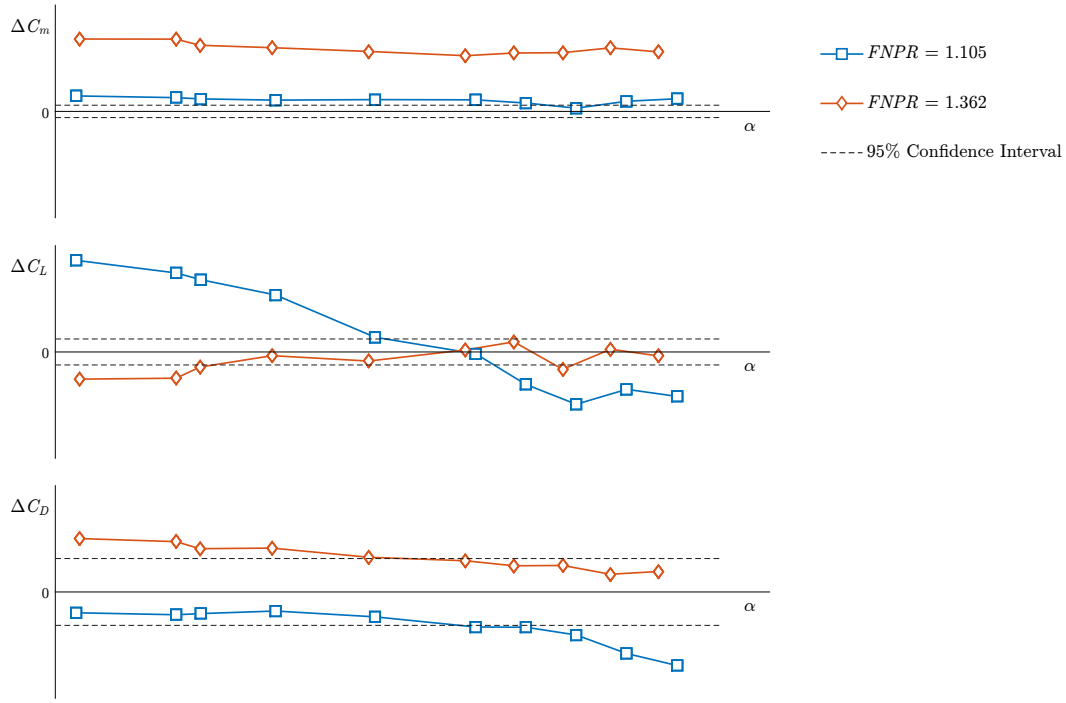

Figure 22. Comparison of differential lift, drag, and pitching moment with the maximum elevon 1/2 deflection (*CN3*). Low power TPS data (*P1*) used as differential reference. Confidence intervals taken from repeatability tests (figure 16).

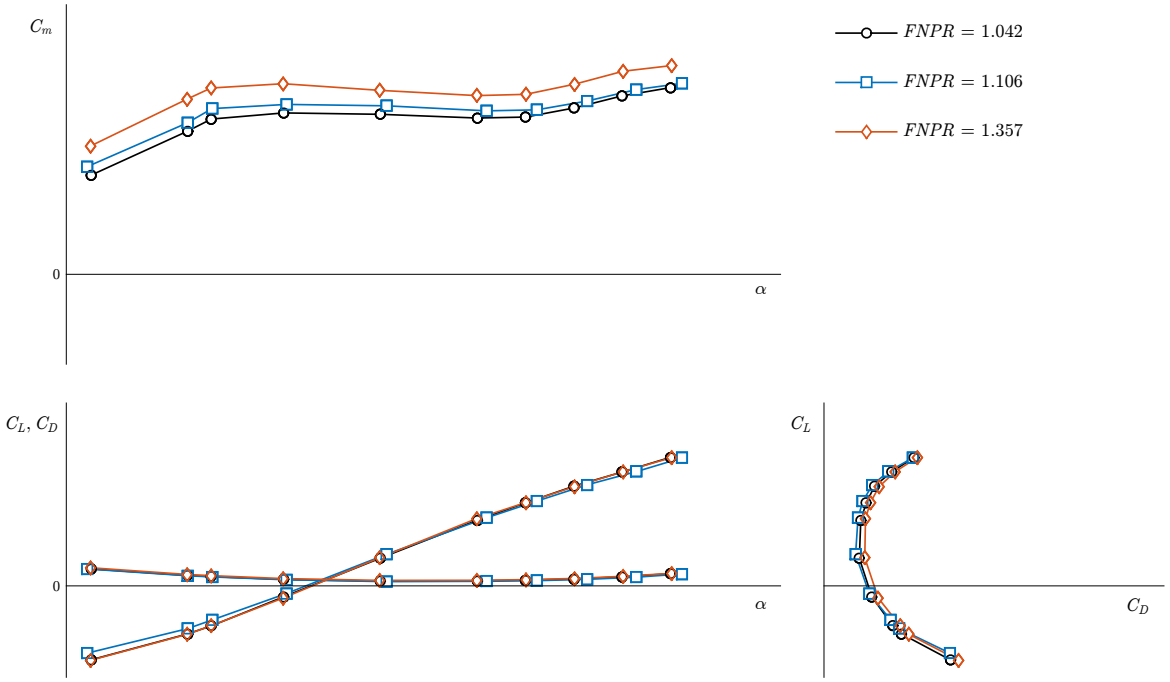

Figure 23. Comparison of TPS power setting effects on lift, drag, and pitching moment with the maximum elevon 1/2 and vertical tail deflections ($CN4$).

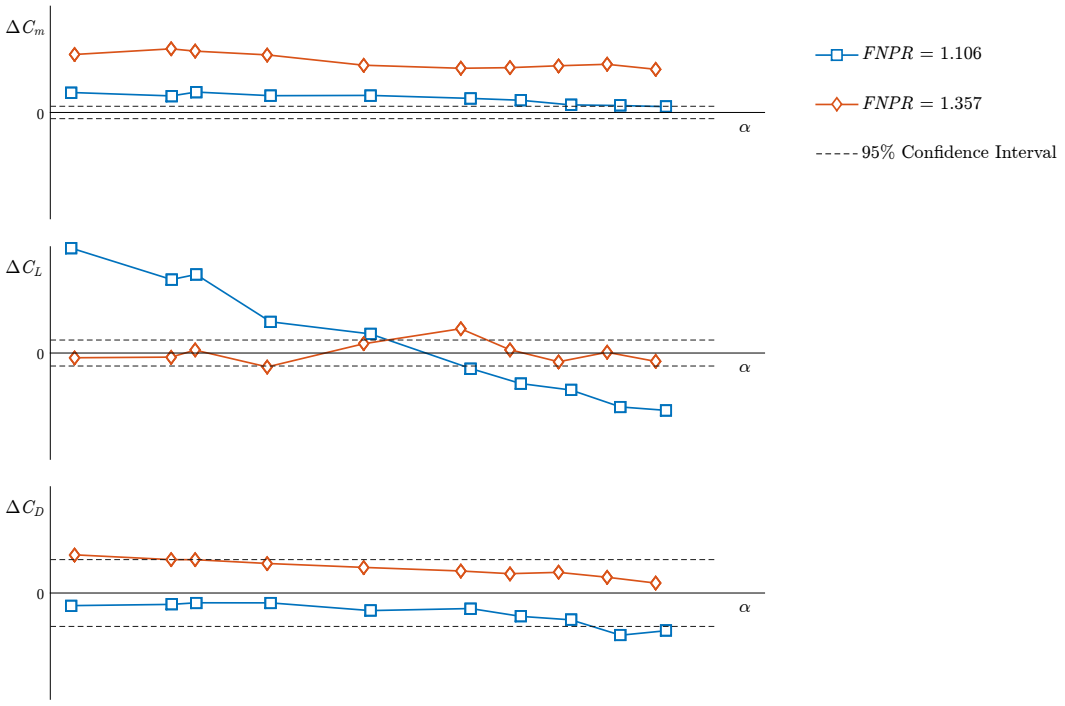

Figure 24. Comparison of differential lift, drag, and pitching moment with the maximum elevon 1/2 and vertical tail deflections ($CN4$). Low power TPS data ($P1$) used as differential reference. Confidence intervals taken from repeatability tests (figure 16).

III.D.4. Control Surface Effects

Figure 25 compares the four control surface settings directly for the high power TPS setting (*P3*) at zero sideslip. As expected, the pitching moment coefficient increases as additional control deflections are applied. Along with this increase in the pitching moment, the drag coefficient increases and the lift coefficient decreases. These trends in C_L and C_D are most likely attributed to flow separation in the vicinity of the highly deflected control surfaces which degrades the lift on the centerbody and increases drag. Elevon 1/2 was instrumented for surface pressure measurements that may provide more insight into the C_L and C_D trends, but these data are still being evaluated.

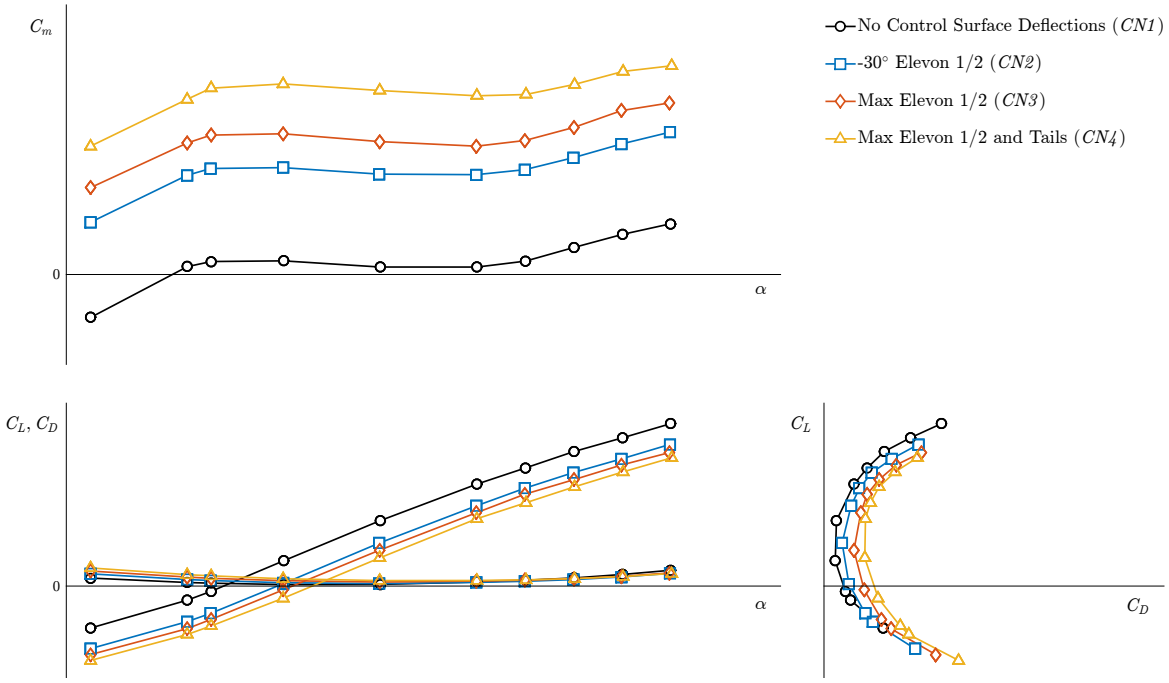

Figure 25. Comparison of TPS control surface effects on lift, drag, and pitching moment at high power TPS setting (*P3*).

A pretest hypothesis was that the blowing effect of the TPS units over the centerbody control surfaces would increase the control surface effectiveness as related to pitching moment. To evaluate this, differential plots are shown below (figures 26–28) comparing the increments with the control surface deflections (*CN2*, *CN3*, and *CN4*) to the no control surface deflection (*CN1*) configurations. The FTN runs are referenced to the FTN no control surface deflection configuration and the TPS runs are referenced to the TPS no control surface deflection configuration. As hypothesized, the pitching moment coefficient increases with the TPS units operating although the effect is not as significant for the -30° elevon 1/2 deflection configuration (*CN2*). Similarly, the blowing from the TPS units is seen to exacerbate the lift deficit for the *CN3* and *CN4* configurations.

The effects of the control surfaces on the drag coefficient are more complex as the drag profile (seen in the lower left of figure 25) effectively rotates about a particular angle of attack. As such, the drag can either increase or decrease with the control surfaces depending on the pitch angle. The blowing from the TPS units increases the pitch angle that the drag profile rotates about, shifting the differential curves (figure 28) up and to the right while decreasing slope.

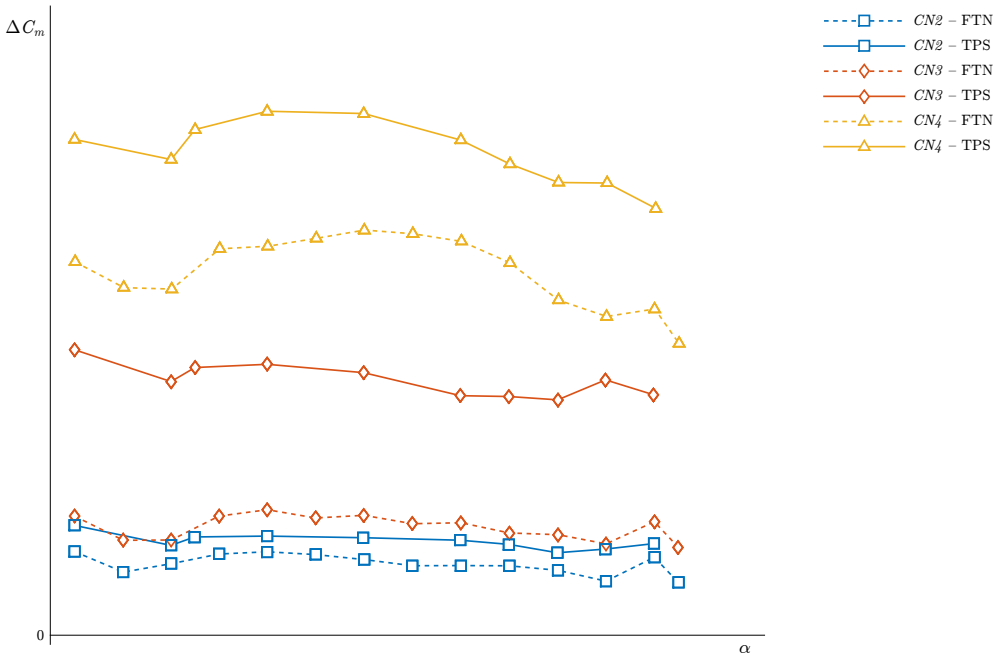

Figure 26. Comparison of FTN and TPS control surface deflection effects on pitching moment coefficient. Respective data (FTN or TPS) with no control surface deflections (*CN1*) used as differential reference.

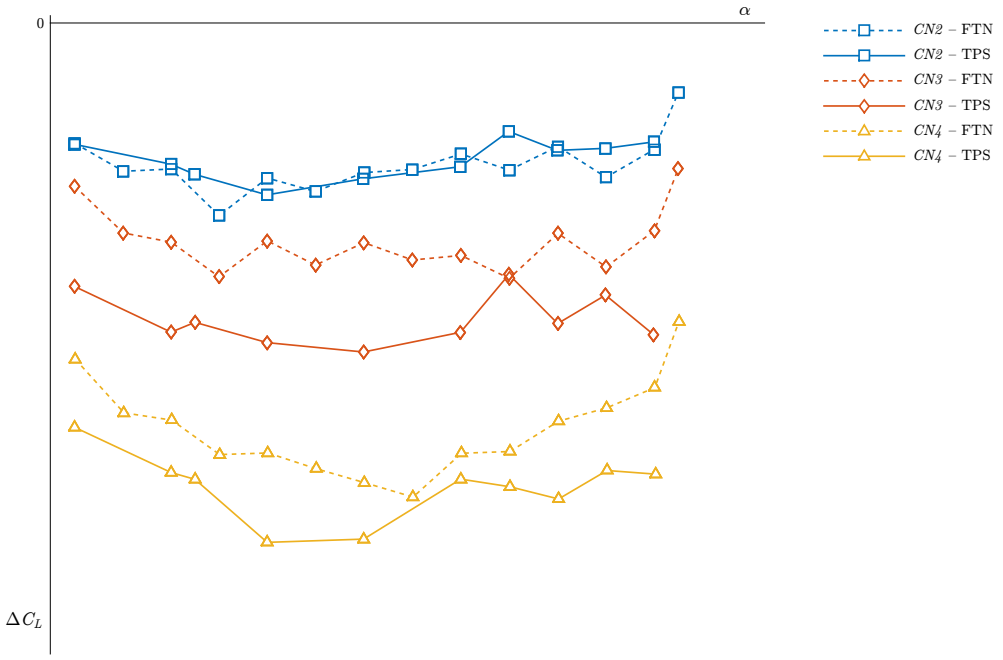

Figure 27. Comparison of FTN and TPS control surface deflection effects on lift coefficient. Respective data (FTN or TPS) with no control surface deflections (*CN1*) used as differential reference.

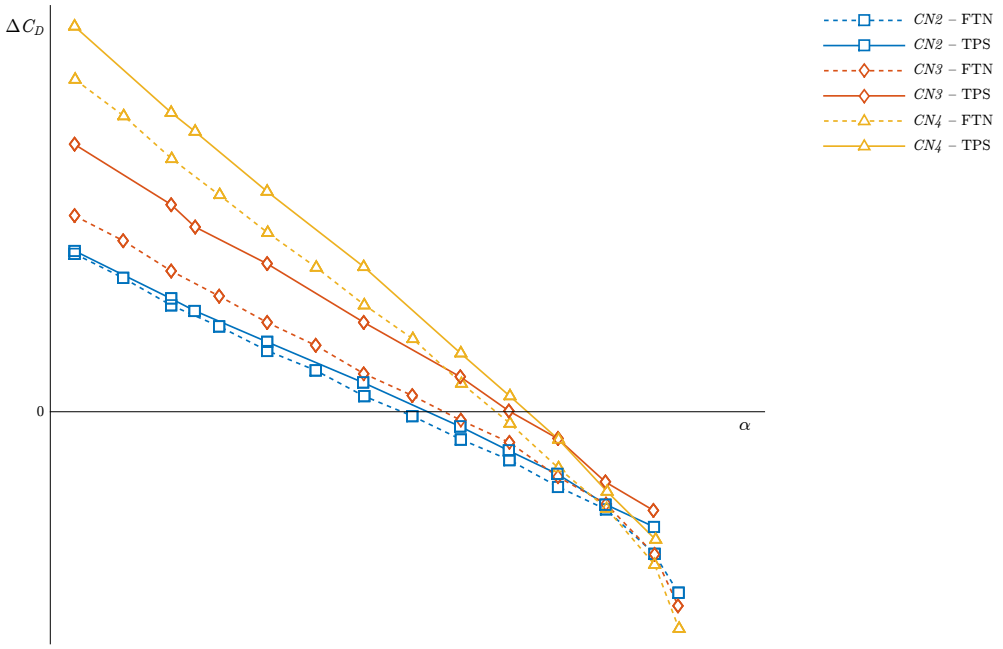

Figure 28. Comparison of FTN and TPS control surface deflection effects on drag coefficient. Respective data (FTN or TPS) with no control surface deflections (*CN1*) used as differential reference.

III.D.5. TPS Height Effects

Data were acquired for two TPS height settings above the surface of the HWB model. All of the data presented previously were at the nominal (high) TPS height. The second setting was a lower TPS height. The lower height was predicted to have a greater blowing effect as a result of being closer to the control surfaces, which would further enhance control surface effectiveness. Figures 29–31 compare the C_m, C_L, and C_D increments for the two height settings. The increments are again relative to the respective configurations with no control surface deflections (*CN1*).

Looking first at pitching moment (figure 29), the control surface increments are seen to increase significantly for the low TPS height when compared to the high height as expected. Note that the full elevon 1/2 and tail deflection configuration (*CN4*) is not reported as the mass flow-through the fan at higher angles of attack was not sufficient to cool the TPS bearings at the lower TPS height. Comparing the lift coefficient for the two TPS heights (figure 30), the lower TPS setting is again seen to enhance the control surface effects by decreasing the lift coefficient. It is interesting to note that lift decreases at the lower TPS height for the -30° elevon 1/2 deflection configuration (*CN2*), as a significant change in the increment was not seen for the higher TPS setting and the FTN configurations (figure 27). The results for drag coefficient (figure 31) are not as consistent. For the -40° elevon 1/2 deflection configuration (*CN3*), the drag coefficient increment is seen to shift up on the ΔC_D vs. α plot and the slope of the line increases negatively. The changes in increment for the -30° elevon 1/2 deflection configuration (*CN2*) for the high and low TPS heights are nearly the same across the angle-of-attack range investigated, and small differences are most likely within the measurement uncertainty.

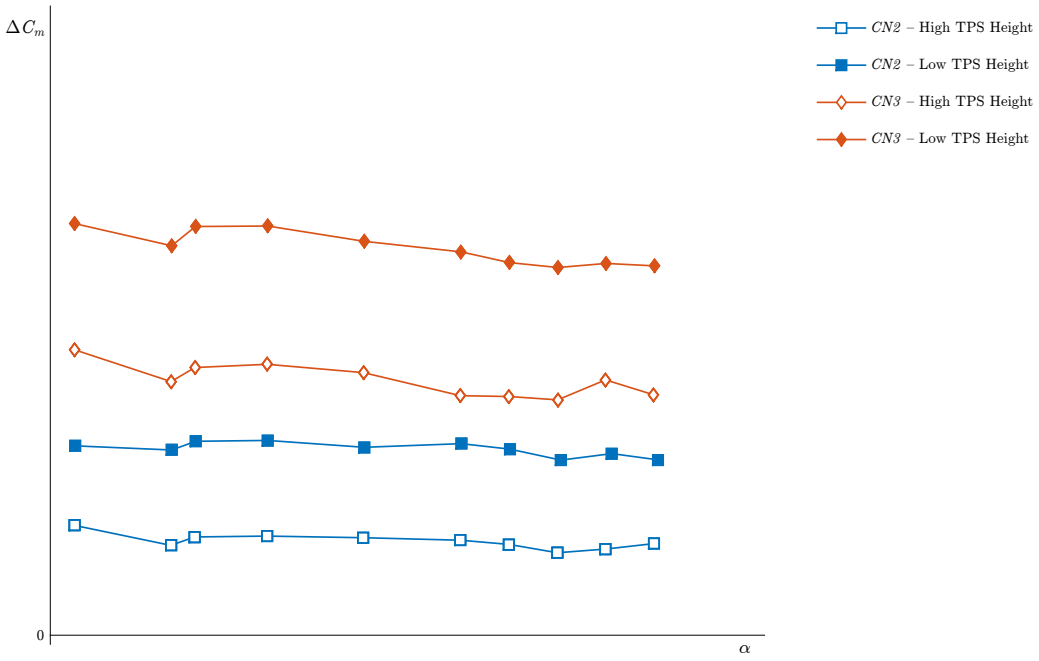

Figure 29. Comparison of control surface deflection effects on pitching moment coefficient for two TPS height settings. Respective data (high or low) with no control surface deflections (*CN1*) used as differential reference.

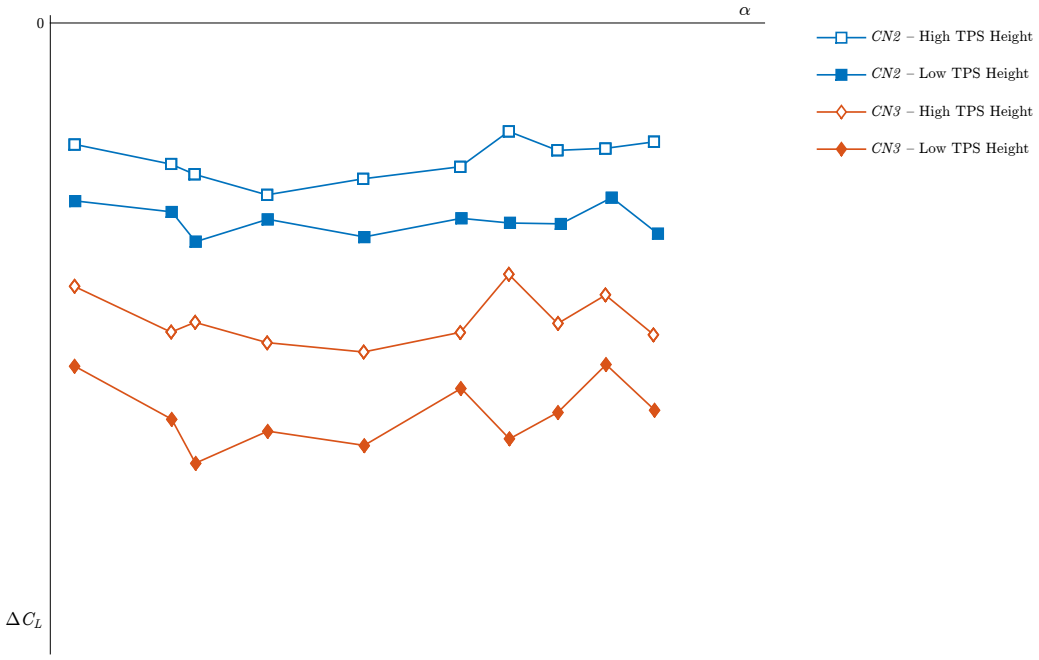

Figure 30. Comparison of control surface deflection effects on lift coefficient for two TPS height settings. Respective data (high or low) with no control surface deflections (*CN1*) used as differential reference.

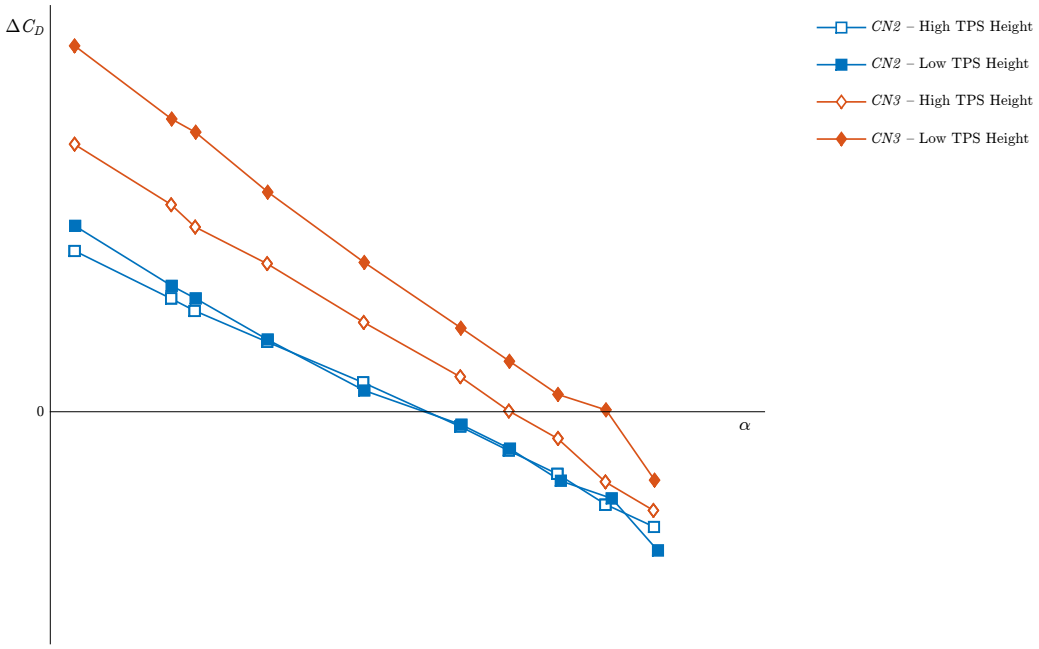

Figure 31. Comparison of control surface deflection effects on drag coefficient for two TPS height settings. Respective data (high or low) with no control surface deflections (*CN1*) used as differential reference.

IV. Conclusions

Calibration of three turbine powered simulators was completed in the NASA Ames UPWT 9- by 7-foot Supersonic Test Section. Each of the motors were found to have similar operational characteristics which was ideal for the hybrid wing body integration testing with two units. The results of the calibration tests were used to develop mapping algorithms for the TPS unit resultant force and fan weight flow as functions of the motor speed (rpm) and fan nozzle pressure ratio. These mapping algorithms were used for reducing the aerodynamic measurements from the integration testing on the hybrid wing body where the resultant force and weight flow could not be measured directly, but were required to calculate aerodynamic forces and moments specific to the TPS units.

Propulsion airframe integration testing on the hybrid wing body using turbine powered simulators was completed at the National Full-Scale Aerodynamics Complex 40- by 80-foot test section. Four rear control surface configurations were tested with the TPS units to investigate how the jet exhaust from the TPS units influenced the control surface performance. Compared to flow-through nacelle testing on the same HWB model, the control surface effectiveness increased with the TPS units operating. This was true for pitching moment, lift, and drag although pitching moment was the parameter of greatest interest for the current tests. With the TPS units operating, pitching moment was seen to increase when compared to the FTN configuration as desired.

Data were acquired at two TPS heights above the surface of the HWB model. As predicted, the lower TPS height was seen to enhance the control surface effects as a result of the increased blowing over the center elevon. Although this is a positive result from the perspective of stability and control, the improved control surface performance must be balanced with engine performance and acoustics in a comprehensive airframe design. The nominal (high) placement is expected to provide better engine performance over a wide range of operating conditions as moving the engines away from the surface of the airframe decreases the possibility of the inlets being enveloped in separated flow at higher angles of attack.

Measurement uncertainty was evaluated by performing repeatability runs throughout the course of testing. The increments measured for pitching moment were well outside the data repeatability bounds providing confidence in the aerodynamic effects measured. Lift and drag increments were not clearly outside the bounds of the repeatability, but consistent trends were seen throughout testing for the various control configurations.

As such, the trends seen in the C_L and C_D increments are most likely physical. To develop more confidence in the magnitudes of the increments, a more sensitive balance would be required.

Acknowledgments

The authors would like to thank the test teams from the NASA Ames Unitary Plan Wind Tunnel and the National Full-Scale Aerodynamics Complex for their support of the tests and data processing. Furthermore, the authors would like to thank the members of ERA ITD-51A research team for their insight and cooperative efforts, and acknowledge the NASA Environmentally Responsible Aviation Project for sponsoring this research.

References

[1]Liebeck, R. H., "Design of the Blended Wing Body Subsonic Transport," *Journal of Aircraft*, Vol. 41, No. 1, January-February 2004, pp. 10–25.

[2]Campbell, R. L., Carter, M. B., Pendergraft Jr., O. C., Friedman, D. M., and Serrano, L., "Design and Testing of a Blended Wing Body with Boundary Layer Ingestion Nacelles at High Reynolds Numbers (Invited)," AIAA Paper 2005-0459, 43rd AIAA Aerospace Sciences Mtg., 10–13 January 2005, Reno, NV.

[3]Carter, M. B., Campbell, R. L., Pendergraft Jr., O. C., Friedman, D. M., and Serrano, L., "Designing and Testing a Blended Wing Body with Boundary-Layer Ingestion Nacelles," *Journal of Aircraft*, Vol. 43, No. 5, 2006, pp. 1479–1489.

[4]Vicroy, D. D., "Blended-Wing-Body Low-Speed Flight Dynamics: Summary of Ground Tests and Sample Results (Invited)," AIAA Paper 2009-0933, 47th AIAA Aerospace Sciences Mtg., 5–8 January 2009, Orlando, FL.

[5]Carter, M. B., Vicroy, D. D., and Patel, D., "Blended-Wing-Body Transonic Aerodynamics: Summary of Ground Tests and Sample Results (Invited)," AIAA Paper 2009-0935, 47th AIAA Aerospace Sciences Mtg., 5–8 January 2009, Orlando, FL.

[6]Gatlin, G. M., Vicroy, D. D., and Carter, M. B., "Experimental Investigation of the Low-Speed Aerodynamic Characteristics of a 5.8-Percent Scale Hybrid Wing Body Configuration," AIAA Paper 2012-2669, 30th AIAA Applied Aerodynamics Conference, 25–28 June 2012, New Orleans, LA.

[7]Vicroy, D. D., Gatlin, G. M., Jenkins, L. N., Murphy, P. C., and Carter, M. B., "Low-speed Aerodynamic Investigations of a Hybrid Wing Body Configuration," AIAA Paper 2014-2563, 32nd AIAA Applied Aerodynamics Conference, 16–20 June 2014, Atlanta, GA.

[8]Dickey, E. D., Princen, N. H., Bonet, J. T., and Ige, G. K., "Wind Tunnel Model Design and Fabrication of a 5.75% Scale Blended-Wing-Body Twin Jet Configuration," 54th AIAA Aerospace Sciences Mtg., 4–8 January 2016, San Diego, CA.

[9]Vicroy, D. D., Dickey, E. D., Princen, N. H., and Beyar, M. D., "Overview of Low-speed Aerodynamic Tests on a 5.75% Scale Blended-Wing-Body Twin Jet Configuration," 54th AIAA Aerospace Sciences Mtg., 4–8 January 2016, San Diego, CA.

[10]Carter, M. B., Shea, P. R., Flamm, J. D., Schuh, M., James, K. D., Sexton, M. R., Tomkins, D. M., and Beyar, M. D., "Experimental Evaluation of Inlet Distortion on an Ejector Powered Hybrid Wing Body at Take-off and Landing Conditions," 54th AIAA Aerospace Sciences Mtg., 4–8 January 2016, San Diego, CA.

[11]Hammond, A. D. and Johnson, C. B. G. J., "Development of Wind-Tunnel Test Techniques for Propulsion System Simulators for Use in Small-Scale V/STOL Models," ASME Joint Conference of the Gas Turbine Division and Fluids Engineering Division, 26–30 March 1972, San Francisco, CA.

[12]Gentry Jr., G. L., Takallu, M. A., and Applin, Z. T., "Aerodynamic Characteristics of a Propeller-Powered High-Lift Semispan Wing," NASA Technical Memorandum 4541, 1994.

[13]Thomas, R. H., Gerhold, C. H., Farrasat, F., Maria, O. L. S., Nuckolls, W. E., and Vilbiss, D. W. D., "Far Field Noise of the 12 Inch Advanced Ducted Propeller Simulator," AIAA Paper 1995-0722, 33rd AIAA Aerospace Sciences Meeting, 9–12 January 1995, Reno, NV.

[14]Hoheisel, H., *Performance Data of a Counter Rotating Ultra High Bypass Engine Simulator*, Deutsches Zentrum für Luft- und Raumfahrt, 1998.

[15]Tompkins, D. M., Long, K. R., Flamm, J. D., and James, K. D., "Experimental Validation of Modifications to a TDI Model 2700 Turbine Powered Simulator to Simulate a High-Bypass Ratio Engine," AIAA Paper 2014-3888, 50th AIAA/ASME/SAE/ASEE Joint Propulsion Conference, 28–30 July 2014, Cleveland, OH.

[16]Roberts, A. C. and Smith, K. M., "Development of a new flow-through force measurement balance with improved accuracy for use in powered wind tunnel model testing," AIAA Paper 1988-2059, 15th AIAA Aerodynamic Testing Conference, 18–20 May 1988, San Diego, CA.

[17]Melton, J. E., James, K. D., Long, K. R., and Flamm, J. D., "Estimating Flow-Through Balance Momentum Tares with CFD," 54th AIAA Aerospace Sciences Mtg., 4–8 January 2016, San Diego, CA.

[18]Zell, P. T. and Flack, K., "Performance and Test Section Flow Characteristics of the National Full-Scale Aerodynamics Complex 40- by 80-Foot Wind Tunnel," NASA Technical Memorandum 101065.

[19]Soderman, P. T., Jaeger, S. M., Hayes, J. A., and Allen, C. S., "Acoustic Quality of the 40- by 80-Foot Wind Tunnel Test Section After Installation of a Deep Acoustic Lining," NASA Technical Publication 2002-211851.

[20]Hunt, R. and Sacco, J., "Activation and Operation of the National Full-Scale Aerodynamics Complex," AIAA Paper 2000-1076, 38th Aerospace Sciences Mtg., 10–13 January 2000, Reno, NV.

[21]Murakami, D. D., Long, K. R., and Schery, S. D., "High Accuracy Total Temperature Measurements in a Turbine Powered Simulator Unit," AIAA 2015-4197, 51st AIAA/SAE/ASEE Joint Propulsion Conference, 27–29 July 2015, Orlando, FL.